deranged cardiac excitability, from conduction disease to sudden cardiac death. □

Methods

Sequence analysis, mutagenesis and transfection

The entire coding region of *SCN5A* was screened by SSCP and direct sequence analysis as described[19], and site-directed mutagenesis was performed on *SCN5A* complementary DNA cloned into the green fluorescent protein (GFP) expression vector pCGI (ref. 20) as described[21]. Cultured cells (tsA201) were co-transfected with a 5:1 molar ratio of the Na^+-channel β_1 subunit (provided by A. George, Vanderbilt University).

Electrophysiology

Unless otherwise indicated, I_{Na} was recorded at room temperature (22 °C) to optimize voltage-clamp control using established recording conditions[7]. For all voltage-clamp experiments, the pipette solution contained (in mM): NaF 10, CsF 110, CsCl 20, EGTA 10 and HEPES 10 (pH 7.35 with CsOH), and the bath solution contained: NaCl 145, KCl 4, $CaCl_2$ 1.8, $MgCl_2$ 1, HEPES-NaOH pH 7.35. For voltage-dependent activation (Fig. 2c), relative conductance was calculated by dividing the peak I_{Na} at each clamp potential by the driving force (clamp voltage minus measured reversal potential), then normalizing to the value at 0 mV. For voltage-dependent inactivation (Fig. 3a), relative currents were calculated by normalizing peak I_{Na} (elicited by depolarization to −20 mV) to the value recorded after holding at the most negative (−120 mV) conditioning voltage. The rate of development of closed-state inactivation (Fig. 3b) was analysed using variable duration pre-pulses to −90 or −100 mV. The kinetics of recovery from inactivation (Fig. 4a) were assessed using a three-pulse clamp protocol. The ratio of the peak I_{Na} elicited by the P_2 pulse, relative to the P_1 pulse, was plotted as a function of the intervening recovery interval at −140 mV.

Action potential simulations

The Luo–Rudy model[10,22,23] of a mammalian ventricular myocyte action potential provided the basis for the action potential simulations (Fig. 5), with I_{to} added as described[6]. A one-dimensional fibre[10] consisting of endocardial (cells 1–80), midmyocardial (81–110), and epicardial (111–190) cells was used to mimic *in vivo* conditions. A stimulus was applied to cell no. 1 to simulate normal endocardial to epicardial impulse propagation.

Received 22 November; accepted 21 December 2000.

1. Wang, Q. *et al. SCN5A* mutations associated with an inherited cardiac arrhythmia, long QT syndrome. *Cell* **80,** 805–811 (1995).
2. Bennett, P. B., Yazawa, K., Naomasa, M. & George, A. L. Molecular mechanism for an inherited cardiac arrhythmia. *Nature* **376,** 683–685 (1995).
3. Chen, Q. *et al.* Genetic basis and molecular mechanism for idiopathic ventricular fibrillation. *Nature* **392,** 293–296 (1998).
4. Noda, M. *et al.* Expression of functional sodium channels from cloned cDNA. *Nature* **322,** 826–828 (1986).
5. Horn, R., Patlak, J. B. & Stevens, C. F. Sodium channels need not open before they inactivate. *Nature* **291,** 426–427 (1981).
6. Dumaine, R. *et al.* Ionic mechanisms responsible for the electrocardiographic phenotype of the Brugada syndrome are temperature dependent. *Circ. Res.* **85,** 803–809 (1999).
7. Veldkamp, M. W. *et al.* Two distinct congenital arrhythmias evoked by a multidysfunctional Na^+ channel. *Circ. Res.* **86,** E91–E97 (2000).
8. Deschenes, I. *et al.* Electrophysiological characterization of SCN5A mutations causing long QT (E1784K) and Brugada (R1512W and R1432G) syndromes. *Cardiovasc. Res.* **46,** 55–65 (2000).
9. Priori, S. G. *et al.* Genetic and molecular basis of cardiac arrhythmias: impact on clinical management parts I and II. *Circulation* **99,** 518–528 (1999).
10. Viswanathan, P. C., Shaw, R. M. & Rudy, Y. Effects of IKr and IKs heterogeneity on action potential duration and its rate dependence: a simulation study. *Circulation* **99,** 2466–2474 (1999).
11. Dominguez, G. & Fozzard, H. A. Influence of extracellular K+ concentration on cable properties and excitability of sheep cardiac Purkinje fibers. *Circ. Res.* **26,** 565–574 (1970).
12. Cascio, W. E., Johnson, T. A. & Gettes, L. S. Electrophysiologic changes in ischemic ventricular myocardium: I. Influence of ionic, metabolic, and energetic changes. *J. Cardiovasc. Electrophysiol.* **6,** 1039–1062 (1995).
13. Krishnan, S. C. & Antzelevitch, C. Sodium channel block produces opposite electrophysiological effects in canine ventricular epicardium and endocardium. *Circ. Res.* **69,** 277–291 (1991).
14. Yan, G. X. & Antzelevitch, C. Cellular basis for the Brugada syndrome and other mechanisms of arrhythmogenesis associated with ST-segment elevation. *Circulation* **100,** 1660–1666 (1999).
15. Alings, M. & Wilde, A. "Brugada" syndrome: clinical data and suggested pathophysiological mechanism. *Circulation* **99,** 666–673 (1999).
16. Brugada, P. & Brugada, J. Right bundle branch block, persistent ST segment elevation and sudden cardiac death: a distinct clinical and electrocardiographic syndrome. A multicenter report. *J. Am. Coll. Cardiol.* **20,** 1391–1396 (1992).
17. Priori, S. G., Napolitano, C., Giordano, U., Collisani, G. & Memmi, M. Brugada syndrome and sudden cardiac death in children. *Lancet* **355,** 808–809 (2000).
18. Schott, J. J. *et al.* Cardiac conduction defects associate with mutations in SCN5A. *Nature Genet.* **23,** 20–21 (1999).
19. Bezzina, C. *et al.* A single Na^+ channel mutation causing both long-QT and Brugada syndromes. *Circ. Res.* **85,** 1206–1213 (1999).
20. Johns, D. C., Nuss, H. B. & Marban, E. Suppression of neuronal and cardiac transient outward currents by viral gene transfer of dominant negative KV4.2 constructs. *J. Biol. Chem.* **272,** 31598–31603 (1997).
21. Kambouris, N. G. *et al.* Phenotypic characterization of a novel long QT syndrome mutation in the cardiac sodium channel. *Circulation* **97,** 640–644 (1998).
22. Luo, C. H. & Rudy, Y. A dynamic model of the cardiac ventricular action potential. I. Simulations of ionic currents and concentration changes. *Circulation Research* **74,** 1071–1096 (1994).
23. Zeng, J., Laurita, K. R., Rosenbaum, D. S. & Rudy, Y. Two components of the delayed rectifier K^+ current in ventricular myocytes of the guinea pig type. Theoretical formulation and their role in repolarization. *Circ. Res.* **77,** 140–152 (1995).
24. Davignon, A. *et al.* Normal ECG standards for infants and children. *Pediatr. Cardiol.* **1,** 123–152 (1979).

Acknowledgements

Financial support for this study was provided by the Interuniversity Cardiology Institute of Netherlands (H.L.T. and A.A.M.W.), the Dutch Heart Foundation (A.A.M.W.) and the NIH (J.R.B.) We thank S. Stepanovic and M. Hulsbeek for technical assistance, and L. DeFelice, D. Roden, M. Anderson and A. George for helpful discussion.

Correspondence and requests for materials should be addressed to J.R.B. (e-mail: jeff.balser@mcmail.vanderbilt.edu).

The voltage-sensitive sodium channel is a bell-shaped molecule with several cavities

Chikara Sato*, Yutaka Ueno*, Kiyoshi Asai*, Katsutoshi Takahashi†, Masahiko Sato‡, Andreas Engel§ & Yoshinori Fujiyoshi‖

* *Supermolecular Science Division, Electrotechnical Laboratory (ETL), Umezono 1-1-4, Tsukuba, 305-8568 Japan*
† *School of Knowledge Science, Japan Advanced Institute of Science and Technology Hokuriku (JAIST), Asahidai 1-1, Tatsunokuchi, Ishikawa, 923-1211, Japan*
‡ *Central Research Institute, Itoham Foods Inc., Kubogaoka 1-2, Moriya, 302-0104, Japan*
§ *Maurice E. Müller Institute, at the Biozentrum, University of Basel, Klingelbergstrasse 70, CH-4056 Basel, Switzerland*
‖ *Department of Biophysics, Faculty of Science, Kyoto University, Oiwake, Kitashirakawa, Sakyo-ku, Kyoto, 606-8502, Japan*

Voltage-sensitive membrane channels, the sodium channel, the potassium channel and the calcium channel operate together to amplify, transmit and generate electric pulses in higher forms of life. Sodium and calcium channels are involved in cell excitation, neuronal transmission, muscle contraction and many functions that relate directly to human diseases[1–4]. Sodium channels—glycosylated proteins with a relative molecular mass of about 300,000 (ref. 5)—are responsible for signal transduction and amplification, and are chief targets of anaesthetic drugs[6] and neurotoxins[1]. Here we present the three-dimensional structure of the voltage-sensitive sodium channel from the eel *Electrophorus electricus*. The 19 Å structure was determined by helium-cooled cryo-electron microscopy and single-particle image analysis of the solubilized sodium channel. The channel has a bell-shaped outer surface of 135 Å in height and 100 Å in side length at the square-shaped bottom, and a spherical top with a diameter of 65 Å. Several inner cavities are connected to four small holes and eight orifices close to the extracellular and cytoplasmic membrane surfaces. Homologous voltage-sensitive calcium and tetrameric potassium channels, which regulate secretory processes and the membrane potential[7], may possess a related structure.

Different approaches have provided information on the structure of the sodium channel. Its function and folding topology have been assessed by site-directed mutagenesis[8,9] and peptide-specific antibody binding[10,11]. The structure of a synthetic peptide

corresponding to the III–IV linker (2.6% of the entire molecule) has been analysed by NMR[12], whereas the main features of the solubilized sodium channel have been determined by negative-stain electron microscopy[13]. The structure of a bacterial potassium channel KcsA mutant, which has 20% of the carboxy terminus deleted, has been solved to a resolution of 3.2 Å by MacKinnon's group[14]. The structure analysis based on X-ray crystallography provided a clear explanation for the ion selectivity of the potassium channel[14]; however, the structure of the entire molecule, which is predicted to have six transmembrane helices per subunit[15–17], is essential to understand the mechanism of voltage gating.

Sodium channel molecules were solubilized from *Electrophorus electricus electroplax*, immunoaffinity purified[13] and imaged by cryo-electron microscopy[18]. The images had a poor signal to noise (S/N) ratio (Fig. 1), because the low contrast inherent to proteins was further decreased by the presence of 20% glycerol and 2 M $MgCl_2$, which were required to stabilize the detergent-solubilized sodium channel. The S/N ratio was improved by aligning and averaging projections of similarly orientated molecules (Fig. 1, row 2). Depending on their orientation in the frozen buffer layer, the sodium channels appeared as either almost-square or wedge-shaped projections. The square projections show a faint central density with a central depression, as well as four massive densities at their corners (Fig. 1a, rows 1 and 2). The wedge-shaped projections are more variable, including various densities at peripheral and central regions (Fig. 1b–d, rows 1 and 2).

We interactively selected particles discernible above the background, and processed them for the three-dimensional (3D) reconstruction using the Imagic V system[19]. A total of 11,991 particles were aligned rotationally and translationally by the reference-free method[20], classified into 240 clusters and averaged. The averages were then refined in several cycles[21]. Because the averaged projection down the channel axis exhibited a pseudo-four-fold symmetry (Fig. 1a, row 2), the initial Euler angles of the cluster averages were determined[22] assuming four-fold symmetry. Subsequently, the structure was refined without any symmetry constraints. The Euler angles of the 240 cluster averages (Fig. 1e) showed the sodium channels to be almost randomly orientated in the frozen buffer layer. Comparison of two independent reconstructions by the Fourier shell correlation documents a resolution of 19 Å (Fig. 1f).

The surface representations in Fig. 1, row 3, display the outer shapes of the protein at viewing angles defined by the Euler angles (noted below each column) of the cluster averages in Fig. 1, row 2. Projections along these directions calculated from the 3D density

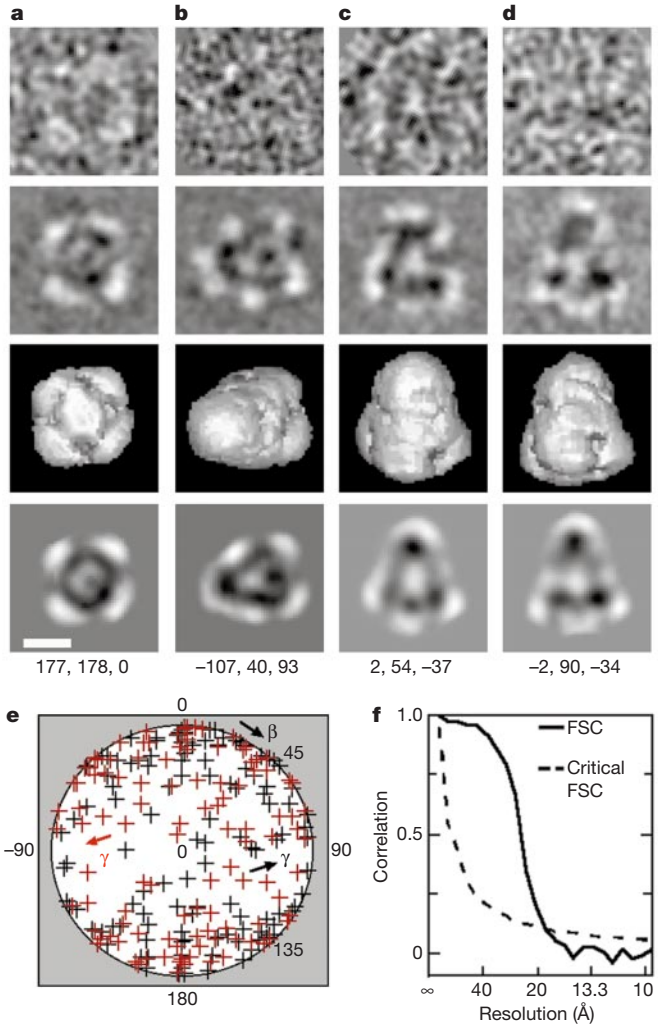

Figure 1 Cryo-electron microscopy of the sodium channel. **a**–**d**, Raw images of molecules with different Euler angles (row 1) are compared with the corresponding 2D averages (row 2), the surface views of the 3D reconstruction (row 3) and the projections of the 3D reconstruction (row 4) along the corresponding Euler directions. Protein is displayed in bright shades. Scale bar, 50 Å. **e**, Surface projection of the Euler angle distribution of the 240 class averages obtained from 11,991 images. Each class average is represented by a cross in a (β, γ) coordinate system. **f**, Fourier shell correlation function between two reconstructions calculated from two half-sets of the data. The cross-over indicates a resolution limit of 19 Å.

map (Fig. 1, row 4) compare well with the experimental averages (Fig. 1, row 2). The isosurface in Fig. 1, row 3, encompasses 150% of the relative molecular mass (M_r) of the channel protein, 208,000 (208K), discounting the glycan moiety that is lost in the averages owing to disorder. At this contouring threshold, four small and four prominent holes penetrate the exterior surface (Fig. 1a–d, row 3). A higher threshold provides a structure with a more complex surface that is difficult to interpret. Examination of the 3D structure over the whole range of Euler angles (Fig. 2) reveals a bell-shaped molecule with a square-shaped end and a narrow top that resembles a half-sphere.

Longitudinal views of the molecule (Figs 1b–d, row 3; and 2) show a 30 Å wide horizontal band without peripheral holes, which probably represents the transmembrane domains (Fig. 2, white lines). Thus, the molecule consists of an upper narrower region corresponding to 24% of the total volume, a transmembrane region (29%), and a lower wider region comprising 47% of the total volume. The relative volumes were estimated using the isosurface shown in Fig. 2. The values for upper and lower regions are in good agreement with those expected from sequence prediction of the extracellular and cytoplasmic domains of the channel molecule (Fig. 3a)[15–17]. Therefore, we tentatively assume that the upper region with its continuous half-spherical outer shell is extracellular, and that the lower region that has prominent orifices dividing it into four unequally sized domains is cytoplasmic (Fig. 2d–f, i). Clockwise from the top left corner of the molecule depicted in Fig. 2a, the relative sizes of these domains are 27, 26, 25 and 22%.

Sections through the 3D density map reveal the internal structure of the voltage-sensitive sodium channel (Fig. 3b–g). Extracellular, transmembrane and cytoplasmic regions tentatively assigned by their surface structure (Fig. 2), and relative volumes (Fig. 3a) are also distinct in the longitudinal sections shown in Fig. 3b–d. The cytoplasmic region houses one central and four peripheral cavities (Fig. 3b–e). The latter have a height and width of roughly 15 Å, and merge with the large cytosolic orifices distinguished in the surface reconstruction (Fig. 2). Four small orifices in the half-spherical extracellular structure (Figs 1–3) perforate the protein shell close to the putative transmembrane region and connect the large internal cavity with the exterior.

The large internal cavities on both the cytoplasmic and extracellular sides connect to four narrow, peripheral, low-density regions in the transmembrane domain (Fig. 3e–g). A rotation of their positions around the pseudo-four-fold axis, about 45° in the upper cross-section (Fig. 3g) relative to the lower cross-section (Fig. 3e), indicates that the low-density feature is twisted. Moreover, each low-density region exhibits a constriction at the level of the arrows in Fig. 3b–d. The distinct elongated central density has a length of 40 Å and a diameter of 35 Å, which is only slightly smaller than the dimensions of the KcsA pore-forming structure[14].

We used antibody labelling of the C19 fragment[13] of the C terminus (residues 1,802–1,820 of the protein sequence)[15] to test the tentative domain assignments. Sodium channel/antibody complexes were separated from excess antibodies by gel-permeation chromatography and examined by negative-stain electron microscopy. The Y-shaped antibodies were often visible on the images, but their conformation was variable (Fig. 4a, b). To identify their binding site, similar end-on and side-view projections were aligned and averaged (Fig. 4c, e), using corresponding average projections of negatively stained sodium channels alone as references (Fig. 4d, f).

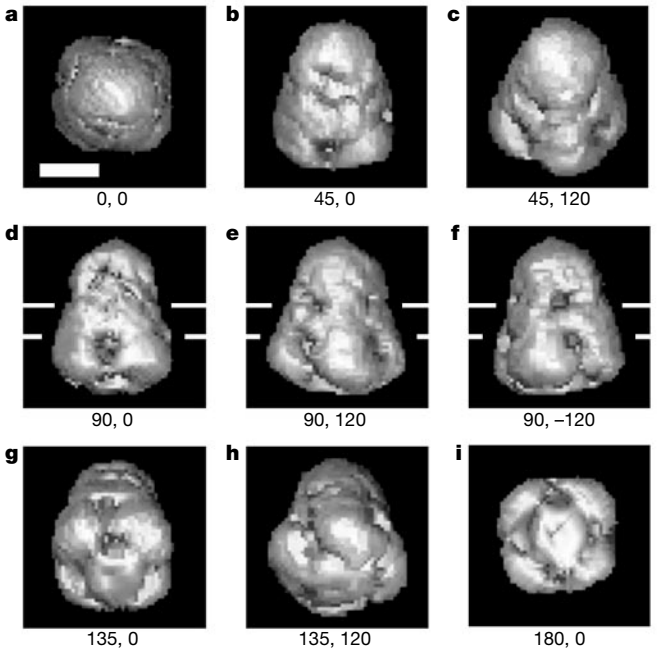

Figure 2 Surface representation of the sodium channel protein. **a**, Top view. **b**, View at an oblique angle, related to **a** by a +45° rotation about the horizontal axis. **c**, View at an oblique angle, related to **b** by a +120° rotation about the vertical axis. **d**–**f**, Three side-views rotated by 120° intervals around the vertical axis. **g**, View at an oblique angle, related to **d** by a +45° rotation about the horizontal axis. **h**, View at an oblique angle, related to **g** by +120° rotation about the vertical axis. **i**, Bottom view. The M_r enclosed by the isosurface is 320K, corresponding to 150% of the sodium channel protein. Euler angles (β, γ) are indicated; the α-angle is 0. White bars delineate the lipid bilayer region. Scale bar, 50 Å.

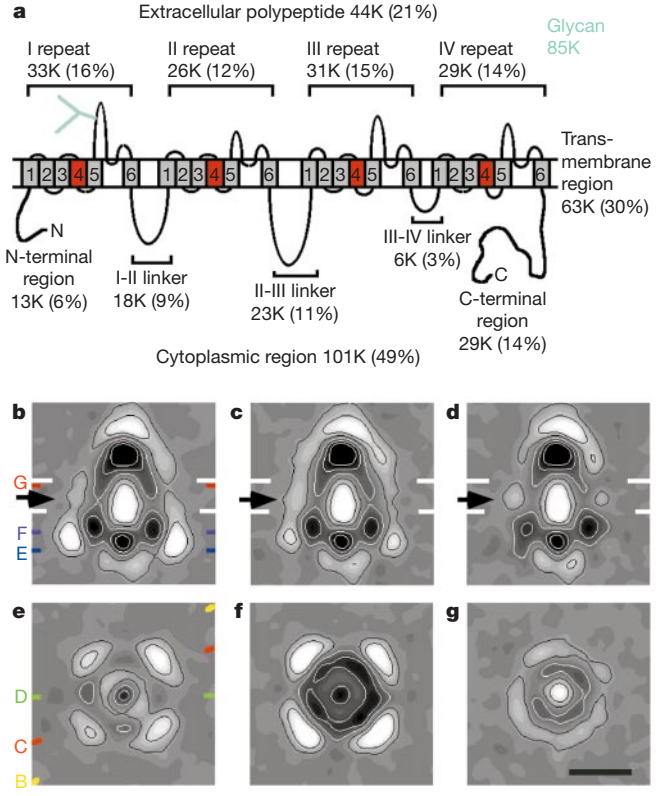

Figure 3 Domains and internal cavities of the sodium channel protein and the sequence-based structure prediction. **a**, Predicted repeats, loops and terminal extensions[5,15]. The S4 segments are colored in red. **b**, Axial section along the diagonal indicated by the yellow line (B) in **e**. **c**, Axial section along the red line (C) in **e**. **d**, Axial section along the green line (D) in **e**. **e**–**g**, Perpendicular sections at the positions marked in **b** by lines coloured blue (E), purple (F) and red (G). High densities are shown in bright shades. White bars delineate the lipid bilayer. Black arrows indicate the constriction between the cytoplasmic (lower) and extracellular (upper) cavities. Scale bar, 50 Å.

Both average projections from the sodium channel/antibody complexes showed densities that could be related to the Fab arms of the antibodies: at the corner of the end-on view (Fig. 4c) and at the edge of the wide end of the side-view (Fig. 4e). The individual Fab domains were blurred, reflecting the flexible nature of the C terminus of the channel. As the C terminus is located on the cytoplasmic side of the membrane[11], the wide, square-shaped end of the sodium channel is indeed located in the cytoplasm.

Whereas voltage-sensitive potassium channels are homotetramers[23], sodium and calcium channels are large monomeric proteins that include four homologous repeats[15,16]. The high sequence homology[15–17] of the transmembrane segments and S5–S6 linkers suggests that these channels share a similar structure. Comparison of the partial structure of KcsA[14] and the lower-resolution 3D density map of the sodium channel presented here indicates that the prominent elongated central density visible in longitudinal sections of the latter (Fig. 3b–d) might correspond to the KcsA pore-forming structure. This is supported by the sequence homology between the KcsA protein and the S5–S6 linker and the S5 and S6 segments of the sodium channel[14]. However, neither the putative channel in the central density nor the features of the central cavity in the transmembrane region[14] is revealed at 19 Å resolution. The low density at the four-fold symmetric axis of the negatively stained sodium channel[13] (Fig. 4) is compatible with our current structure, althouth uranyl salts tend to fill hydrophilic cavities such as those revealed by cryo-electron microscopy. By cryo-electron microscopy, the protein moiety is delineated against the buffer containing 20% glycerol and 2 M $MgCl_2$, yielding a density of 1.185 g ml^{-1}. In contrast, for negatively stained samples flattening, uneven staining and reduced resolution should be considered; these factors explain minor differences between the projections of samples prepared differently.

The cavities and orifices of the sodium channel are unique and may be involved in voltage sensing and gating. In contrast, the acetylcholine receptor exhibits a single funnel-shaped ion inlet on the extracellular side[24]. Cysteine scanning mutagenesis and accessibility tests using hydrophilic cysteine-modifying reagents have shown that only 2–5 residues of the hypothetical transmembrane segment IVS4 (Fig. 3a) are inaccessible[25]. This agrees well with the internal hydrophilic environment created by the cavities. The conservation of hydrophilic residues in the putative transmembrane segments, for example, 36 positively and 22 negatively charged residues, is also compatible with the porous transmembrane structure. Because solubilized sodium channels were not exposed to a membrane potential, they were probably in their closed state on imaging. The short inaccessible hydrophobic region in IVS4 shifts markedly depending on the membrane potential[25]. Conformational changes of the S5–S6 linker have also been observed during outer mouth gating[26]. These observations, together with the presence of a single ion-selective filter revealed by mutagenesis[9] and four voltage sensors[8,15], fosters the hypothesis that the ion pathway is through the elongated central density thought to include S6 (refs 1, 6), and that the pathway is opened by the central mass pushing out into the four surrounding cavities during voltage gating.

The technique that we have used, imaging in the helium-cooled cryo-electron microscope[18] combined with the single particle analysis[19], has provided a low-resolution 3D density map of the sodium channel protein that reveals complex internal cavities and pores. Further improvement of the resolution and structural analysis of sodium channels in the open state are now required to gain more detailed information on the structure of the complex cavity system and the mechanisms of ion transport and gating. □

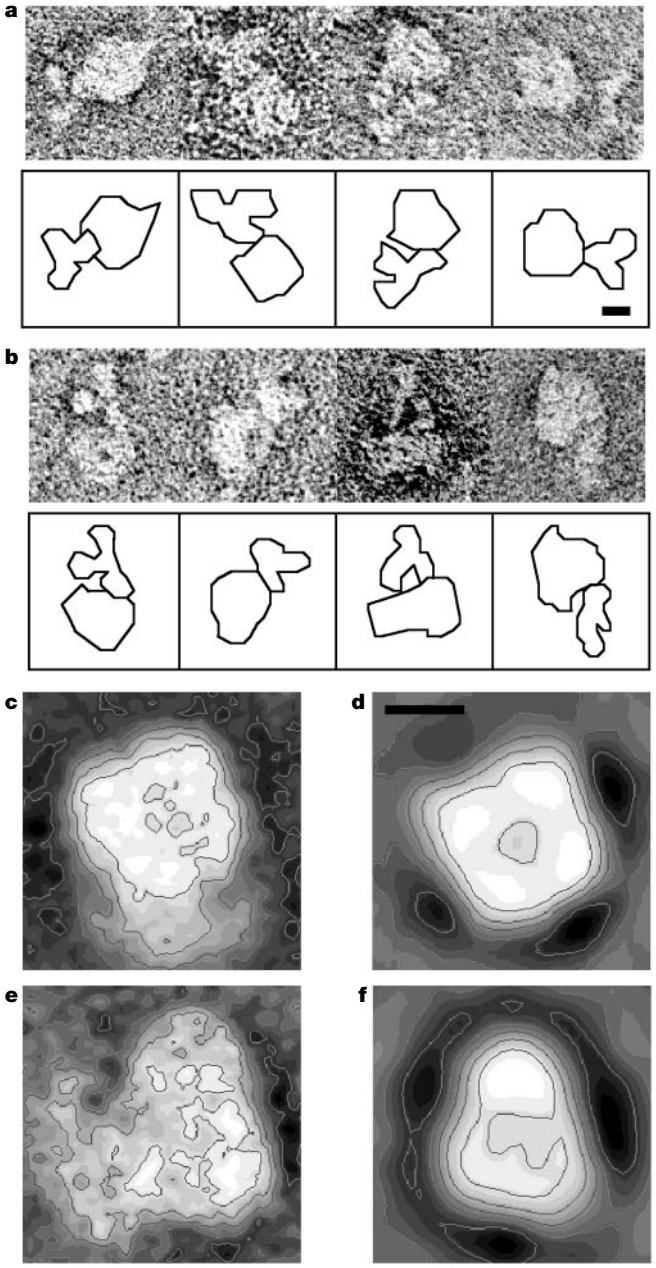

Figure 4 Electron microscopy of negatively stained sodium channel protein, anti-C-terminal antibody complexes and their average projections. **a**, End-on views. **b**, Side views. Contours are shown below each row to delineate the antibody and the sodium channel protein. **c**, **e**, Class averages of the sodium channel protein–antibody complexes; the end-on projection (**c**) shown with contours is the average of 142 projections, and the side view (**e**) is the average of 76 projections. **d**, **f**, Class averages of the sodium channel without antibody; the end-on (**d**) and side-view (**f**) projections are averages containing 196 and 132 projections, respectively. Protein is shown in bright shades. Scale bar, 50 Å.

Methods

Purification of the sodium channels

The voltage-sensitive sodium channel from the electric organ of *Electrophorus electricus* eels was purified by immunoaffinity chromatography and gel filtration as described[13] except that the affinity chromatography gel contained 10 mg ml^{-1} of purified antibody 1A. Elution from the antibody column[13] was achieved by a step gradient containing 3.5 M $MgCl_2$. The subsequent gel permeation chromatography step was carried out as described[13], but with buffer containing 2 M $MgCl_2$. For cryo-electron microscopy, the gel-permeation chromatography fraction of the sodium channels was either used directly or concentrated 2–3-fold by centrifugation in an Amicon centricon 100.

Cryo-electron microscopy

A 3-μl droplet of the sodium channel solution was applied to a holey carbon grid[18]. The grid was partially blotted with filter paper to remove excess solution, immediately plunged

into liquid ethane chilled by liquid nitrogen, transferred into the JEOL JEM3000SFF cryo-electron microscope[18] and kept at 4.2 K. Low-dose (< 20 electrons per Å^2) images were recorded on Kodak SO163 film at a nominal magnification of ×36,000 and with a 300-kV acceleration voltage. Applied underfocus values were 3.7 to 7.6 μm. Thirty-two images were digitized with a Scitex Leafscan 45 scanner[27] at a pixel size of 2.83 Å at the specimen level. The discernible projection images of the molecule were interactively extracted into 80×80 pixel subframes, and analysed after subtracting the uneven background.

Image analysis

Analysis of images was performed in three major refinement cycles using the Imagic V program system[19]. In the first cycle the selected 11,991 images were first aligned rotationally and translationally, and classified by the reference-free method, and subsequently grouped into 500 clusters by multivariate statistical analysis[28,29]. The resulting averages were used as new references, and the cycle was repeated ten times. In the second cycle, original images were corrected for the contrast transfer function (CTF) of the electron microscope using the parameters Cs 1.6 mm, acceleration voltage 300 kV, Cc 2.2 mm, and aligned with the averages. This further refinement cycle, from the alignment to the generation of references, was repeated eight times. Before the third cycle, orientational Euler angles of the class averages were initially determined from the sinogram[22] of cross-correlation functions assuming a C4 symmetry to obtain a preliminary 3D reconstruction by exact filtered back-projection[30]. For the third cycle, aimed at refining the Euler angles, no symmetry was imposed.

We calculated 189 back-projections in evenly spaced directions from the 3D reconstruction. Each of the 11,991 CTF-corrected images was aligned against all 189 projections and subclustered, providing improved cluster averages, and a new 3D map was generated and projected as above. Again, this cycle was repeated until convergence. The final reconstruction included 11,543 images, 96.3% of the selected images. The isosurface threshold level was chosen to yield an essentially closed surface comprising a total volume of 4×10^5 Å^3. To assess the resolution, independent reconstructions were calculated from two half-sets of the data and assessed by the Fourier shell correlation function[30].

Formation of the channel–antibody complex

The antibody 2B against the carboxy-terminal C19 fragment was prepared as described[13]. Formation of the sodium channel/antibody complex and removal of excessive antibody by gel-permeation chromatography were also carried out as described[13], except that the antibody–sodium channel incubation and gel-permeation buffers were both supplemented with 0.1 M $MgCl_2$ and the incubation with antibody was made for 30 min at 4 °C. Negatively stained samples were recorded, digitized and processed as described[13].

Received 4 September; accepted 22 December 2000.

1. Catterall, W. A. From ionic currents to molecular mechanisms: the structure and function of voltage-gated sodium channels. *Neuron* **26,** 13–25 (2000).
2. McClatchey, A. I. *et al.* Temperature-sensitive mutations in the III–IV cytoplasmic loop region of the skeletal muscle sodium channel gene in paramyotonia congenita. *Cell* **68,** 769–774 (1992).
3. Ptacek, L. J. *et al.* Identification of a mutation in the gene causing hyperkalemic periodic paralysis. *Cell* **67,** 1021–1027 (1991).
4. Deschenes, I. *et al.* Electrophysiological characterization of SCN5A mutations causing long QT (E1784K) and Brugada (R1512W and R1432G) syndromes. *Cardiovasc Res.* **46,** 55–65 (2000).
5. James, W. M. & Agnew, W. S. Multiple oligosaccharide chains in the voltage-sensitive Na^+ channel from *Electrophorus electricus*: evidence for α-2,8-linked polysialic acid. *Biochem. Biophys. Res. Commun.* **148,** 817–826 (1987).
6. Ragsdale, D. S., McPhee, J. C., Scheuer, T. & Catterall, W. A. Molecular determinants of state-dependent block of Na^+ channels by local anesthetics. *Science* **265,** 1724–1728 (1994).
7. Kandel, E. R. & Schwartz, J. H. Molecular biology of learning: modulation of transmitter release. *Science* **218,** 433–443 (1982).
8. Stühmer, W. *et al.* Structural parts involved in activation and inactivation of the sodium channel. *Nature* **339,** 597–603 (1989).
9. Heinemann, S. H., Terlau, H., Stühmer, W., Imoto, K. & Numa, S. Calcium channel characteristics conferred on the sodium channel by single mutations. *Nature* **356,** 441–443 (1992).
10. Vassilev, P. M., Scheuer, T. & Catterall, W. A. Identification of an intracellular peptide segment involved in sodium channel inactivation. *Science* **241,** 1658–1661 (1988).
11. Gordon, R. D., Fieles, W. E., Schotland, D. L., Hogue-Angeletti, R. & Barchi, R. L. Topographical localization of the C-terminal region of the voltage-dependent sodium channel from *Electrophorus electricus* using antibodies raised against a synthetic peptide. *Proc. Natl Acad. Sci. USA* **84,** 308–312 (1987).
12. Rohl, C. A. *et al.* Solution structure of the sodium channel inactivation gate. *Biochemistry* **38,** 855–861 (1999).
13. Sato, C., Sato, M., Iwasaki, A., Doi, T. & Engel, A. The sodium channel has four domains surrounding a central pore. *J. Struct. Biol.* **121,** 314–325 (1998).
14. Doyle, D. A. *et al.* The structure of the potassium channel: molecular basis of K^+ conduction and selectivity. *Science* **280,** 69–77 (1998).
15. Noda, M. *et al.* Primary structure of *Electrophorus electricus* sodium channel deduced from cDNA sequence. *Nature* **312,** 121–127 (1984).
16. Tanabe, T. *et al.* Primary structure of the receptor for calcium channel blockers from skeletal muscle. *Nature* **328,** 313–318 (1987).
17. Tempel, B. L., Papazian, D. M., Schwarz, T. L., Jan, Y. N. & Jan, L. Y. Sequence of a probable potassium channel component encoded at Shaker locus of *Drosophila*. *Science* **237,** 770–775 (1987).
18. Fujiyoshi, Y. The structural study of membrane proteins by electron crystallography. *Adv. Biophys.* **35,** 25–80 (1998).
19. van Heel, M., Harauz, G., Orlova, E. V., Schmidt, R. & Schatz, M. A new generation of the IMAGIC image processing system. *J. Struct. Biol.* **116,** 17–24 (1996).
20. Penczek, P., Radermacher, M. & Frank, J. Three-dimensional reconstruction of single particles embedded in ice. *Ultramicroscopy* **40,** 33–53 (1992).
21. van Heel, M. Classification of very large electron microscopical image data sets. *Optik* **82,** 114–126 (1989).
22. van Heel, M. Angular reconstitution: a posteriori assignment of projection directions for 3D reconstruction. *Ultramicroscopy* **38,** 241–251 (1987).
23. MacKinnon, R. Determination of the subunit stoichiometry of a voltage-activated potassium channel. *Nature* **350,** 232–235 (1991).
24. Miyazawa, A., Fujiyoshi, Y., Stowell, M. & Unwin, N. Nicotinic acetylcholine receptor at 4.6 Å resolution: Transverse tunnels in the channel wall. *J. Mol. Biol.* **288,** 765–786 (1999).
25. Yang, N., George, A. L. Jr & Horn, R. Molecular basis of charge movement in voltage-gated sodium channels. *Neuron* **16,** 113–122 (1996).
26. Liu, Y., Jurman, M. E. & Yellen, G. Dynamic rearrangement of the outer mouth of a K^+ channel during gating. *Neuron* **16,** 859–867 (1996).
27. Mitsuoka, K., Murata, K., Kimura, Y., Namba, K. & Fujiyoshi, Y. Examination of the LeafScan 45, a line-illuminating micro-densitometer, for its use in electron crystallography. *Ultramicroscopy* **68,** 109–121 (1997).
28. van Heel, M. Multivariate statistical classification of noisy images (randomly oriented biological macromolecules). *Ultramicroscopy* **13,** 165–183 (1984).
29. Frank, J., Bretaudiere, J. P., Carazo, J. M., Verschoor, A. & Wagenknecht, T. Classification of images of biomolecular assemblies: a study of ribosomes and ribosomal subunits of *Escherichia coli*. *J. Microsc.* **150,** 99–115 (1988).
30. Harauz, G. & van Heel, M. Exact filters for general geometry three dimensional reconstruction. *Optik* **73,** 146–156 (1986).

Acknowledgements

We thank S. Müller for her illuminating suggestions and help with the manuscript, and M. van Heel, M. Schatz and R. Schmidt for their helpful and constructive advice. T. Moriya promoted the present research. We also thank K. Imoto for discussions, A. Oshima for suggestions and S. Miyazaki for assistance. This work was supported by grants from the ETL, the Japan New Energy and Industrial Technology Development Organization (NEDO), and the Swiss National Science Foundation (to A.E.), and by the Maurice E. Müller Foundation, Switzerland.

Correspondence and requests for materials should be addressed to C.S. (e-mail: tisato@etl.go.jp).

RGS2 regulates signal transduction in olfactory neurons by attenuating activation of adenylyl cyclase III

Srikumar Sinnarajah*, Carmen W. Dessauer†, Deepa Srikumar*, Jun Chen†, John Yuen*, Solomon Yilma‡, John C. Dennis‡, Edward E. Morrison‡, Vitaly Vodyanoy‡ & John H. Kehrl*

** B cell Molecular Biology Section, Laboratory of Immunoregulation, NIAID, NIH, Bethesda, Maryland 20892, USA*
†Department of Integrative Biology and Pharmacology, University of Texas-Houston Medical School, Houston, Texas 77225, USA
‡ Department of Anatomy, Physiology, and Pharmacology, Auburn University, Auburn, Alabama 36849, USA

The heterotrimeric G-protein G_s couples cell-surface receptors to the activation of adenylyl cyclases and cyclic AMP production (reviewed in refs 1, 2). RGS proteins, which act as GTPase-activating proteins (GAPs) for the G-protein α-subunits α_i and α_q, lack such activity for α_s (refs 3–6). But several RGS proteins inhibit cAMP production by G_s-linked receptors[7,8]. Here we report that RGS2 reduces cAMP production by odorant-stimulated olfactory epithelium membranes, in which the α_s family member α_{olf} links odorant receptors to adenylyl cyclase activation[9,10]. Unexpectedly, RGS2 reduces odorant-elicited cAMP production, not by acting on α_{olf} but by inhibiting the activity of adenylyl cyclase type III, the predominant adenylyl cyclase isoform in olfactory neurons. Furthermore, whole-cell voltage clamp recordings of odorant-stimulated olfactory